

# Analysis of Power Losses and the Efficacy of Power Minimization Strategies in Multichannel Electrical Stimulation Systems

F Varkevisser, W A Serdijn and T L Costa

Section Bioelectronics, Department of Microelectronics, Delft University of Technology, Mekelweg 4, 2628CD Delft, The Netherlands

E-mail: {f.varkevisser;w.a.serdijn;t.m.l.dacosta}@tudelft.nl

15 January 2025

**Abstract.** *Objective.* Neuroprosthetic devices require multichannel stimulator systems with an increasing number of channels. However, there are inherent power losses in typical multichannel stimulation circuits caused by a mismatch between the power supply voltage and the voltage required at each electrode to successfully stimulate tissue. This imposes a bottleneck towards high-channel-count devices, which is particularly severe in wirelessly-powered devices. Hence, advances in the power efficiency of stimulation systems are critical. To support these advances, this paper presents a methodology to identify and quantify power losses associated with different power supply scaling strategies in multichannel stimulation systems. *Approach.* The proposed methodology utilizes distributions of stimulation amplitudes and electrode impedances to calculate power losses in multichannel systems. Experimental data from previously published studies spanning various stimulation applications were analyzed to evaluate the performance of fixed, global, and stepped supply scaling methods, focusing on their impact on power dissipation and efficiency. *Main Results.* Variability in output conditions results in low power efficiency in multichannel stimulation systems across all applications. Stepped voltage scaling demonstrated substantial efficiency improvements, achieving an increase of 67% to 146%, particularly in high-channel-count applications with significant variability in tissue impedance. Global scaling, by contrast, was more advantageous for systems with fewer channels. *Significance.* The findings highlight the importance of tailoring power management strategies to specific applications to optimize efficiency while minimizing system complexity. The proposed methodology offers a framework for evaluating efficiency-complexity trade-offs, advancing the design of scalable neurostimulation systems, and supporting future developments in multichannel neuroprosthetic devices.

*Keywords:* Electrical Stimulation, Neuromodulation, Power Efficiency, Power Losses, Supply Scaling, Adaptive Voltage Supply, Multichannel System Design

## 1. Introduction

Implantable neurostimulation devices are widely used to treat neurological disorders such as Parkinson's disease, hearing loss, and visual impairment. Emerging

applications, such as visual and bidirectional somatosensory prostheses, demand large-scale multichannel stimulator systems capable of stimulating hundreds to thousands of channels [1–3]. The development of such systems is a complex interdisciplinary challenge, requiring intricate system- and circuit-level considerations for the electronic circuits [4], and the design of biocompatible high-density electrode interfaces [5]. As the number of stimulation channels continues to scale, the available power becomes a major bottleneck. Traditionally, power is delivered wirelessly to the implantable stimulators since it avoids the infection risks posed by wired connections [6]. However, the power that can be transferred to the implant is limited by several safety regulations, such as the specific absorption rate (SAR) limit [6, 7]. Consequently, optimizing the power efficiency of stimulator circuits is essential to enable further channel scaling and ensure these devices can function effectively within the limits of available power. Furthermore, power losses in the circuits lead to heat generation, which should be minimized to prevent damage to the tissue surrounding the implantable device [8]. Improving power efficiency reduces excessive heating and improves the safety of the device.

Stimulator circuits are typically implemented to allow for current mode stimulation (CMS) or voltage mode stimulation (VMS). CMS is often preferred due to its precise control over injected charge, which is critical for safe stimulation [9, 10]. However, CMS suffers from inherent power inefficiency, as illustrated in figure 1. In a conventional bipolar CMS setup (figure 1a), rectangular current pulses are generated from a fixed voltage supply,  $V_{DD}$ . The stimulation current leads to a voltage drop over the tissue load equal to  $V_{load} = I_{stim}Z_{tissue}$  (figure 1), where  $I_{stim}$  is the stimulation current and  $Z_{tissue}$  the tissue impedance. Any mismatch between  $V_{load}$  and  $V_{DD}$  (indicated in grey in figure 1) leads to excessive power dissipation in the current source, reducing overall efficiency. A possible solution is to scale down the voltage supply, minimizing overhead losses and improving efficiency ( $\eta$ ), as illustrated in figure 1c.

In multichannel systems, however, the variability of tissue impedance and current amplitude between channels complicates this approach. Each channel has different voltage requirements, making the application of voltage scaling more complex [12]. To address this, several voltage scaling strategies are proposed in the literature to reduce the losses at the output driver. The different scaling strategies are illustrated in figure 2 for a system with five channels with varying load voltage requirements. Figure 2a illustrates the conventional approach of using a fixed voltage supply for all channels. Ideally, each channel would have its own dedicated voltage supply precisely matching its load voltage (figure 2b), a strategy often referred to as adiabatic voltage scaling [13, 14]. However, this approach faces scalability limitations, as each channel requires a separate voltage supply, and implementing adiabatic scaling often demands an impractically large chip area, making it unsuitable for scalable solutions. An alternative is to use a single scalable supply (figure 2c) [15, 16], where the supply voltage is configured to accommodate the worst-case channel (Channel 2 in figure 2c). While this ensures high efficiency for the worst-case channel, it can result in significant overhead losses for other channels. Another strategy involves creating  $N$  voltage rails distributed across all channels [17–

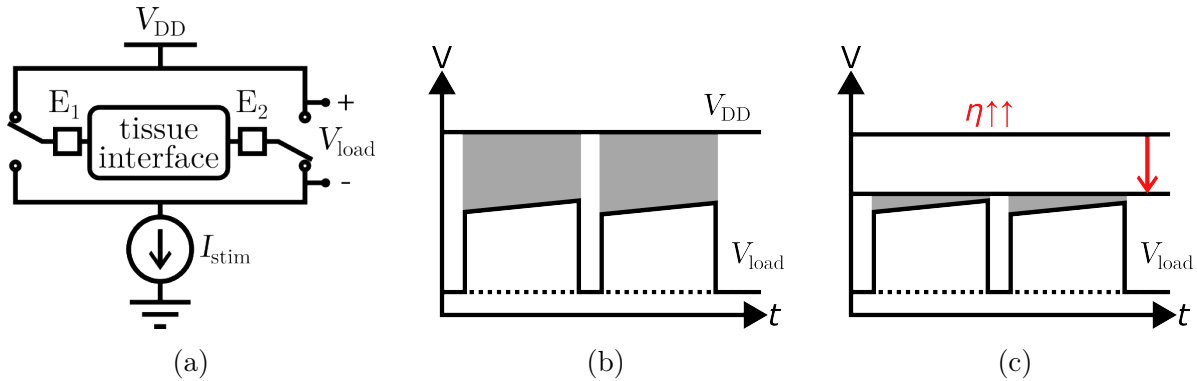


Figure 1: Illustration of the overhead losses in current-mode stimulation (CMS) in a bipolar electrode configuration. (a) Conventional output stage for CMS with a fixed voltage supply  $V_{DD}$ ; (b) Example of the load voltage ( $V_{load}$ ) as a result of the current pulses delivered to the tissue. The mismatch between the load voltage and supply voltage (indicated in the grey area) leads to power dissipation in the output driver; (c) Illustration of how a scaled voltage supply can reduce the power dissipation in the output driver and thus increase the power efficiency, for the example in (b).

20], with each channel connected to the nearest rail above its load voltage (figure 2d). This approach offers a trade-off between power efficiency and system complexity with the choice of  $N$ .

The impact of inter-channel variability on the power efficiency of multichannel stimulation systems is often neglected in conventional designs. This work introduces a novel methodology that incorporates these effects to evaluate the efficacy of various supply scaling strategies and quantify the associated power losses. Using experimental data from various multichannel stimulation applications, the methodology calculates channel-specific load voltage requirements and estimates the overhead losses for different voltage scaling strategies. The results provide valuable insights into the trade-offs between power efficiency and design complexity, offering a systematic framework to guide circuit design considerations for large-scale neurostimulation systems.

## 2. Methods

### 2.1. Data Collection and Extraction

Experimental data was collected using a systematic search in the Scopus database for studies on (micro)stimulation. Inclusion criteria required that the selected studies report (perception) thresholds and impedance data and that the subjects are either humans or non-human primates. For some cases with partially available data, the authors were contacted to request additional data. We collected 26 datasets from 7 publications, spanning four applications. The results are organized by application, resulting in categories for intracortical visual prostheses (V1), retinal implants, intrafascicular peripheral nerve stimulation (iPNS), and extraneural PNS. The extracted datasets

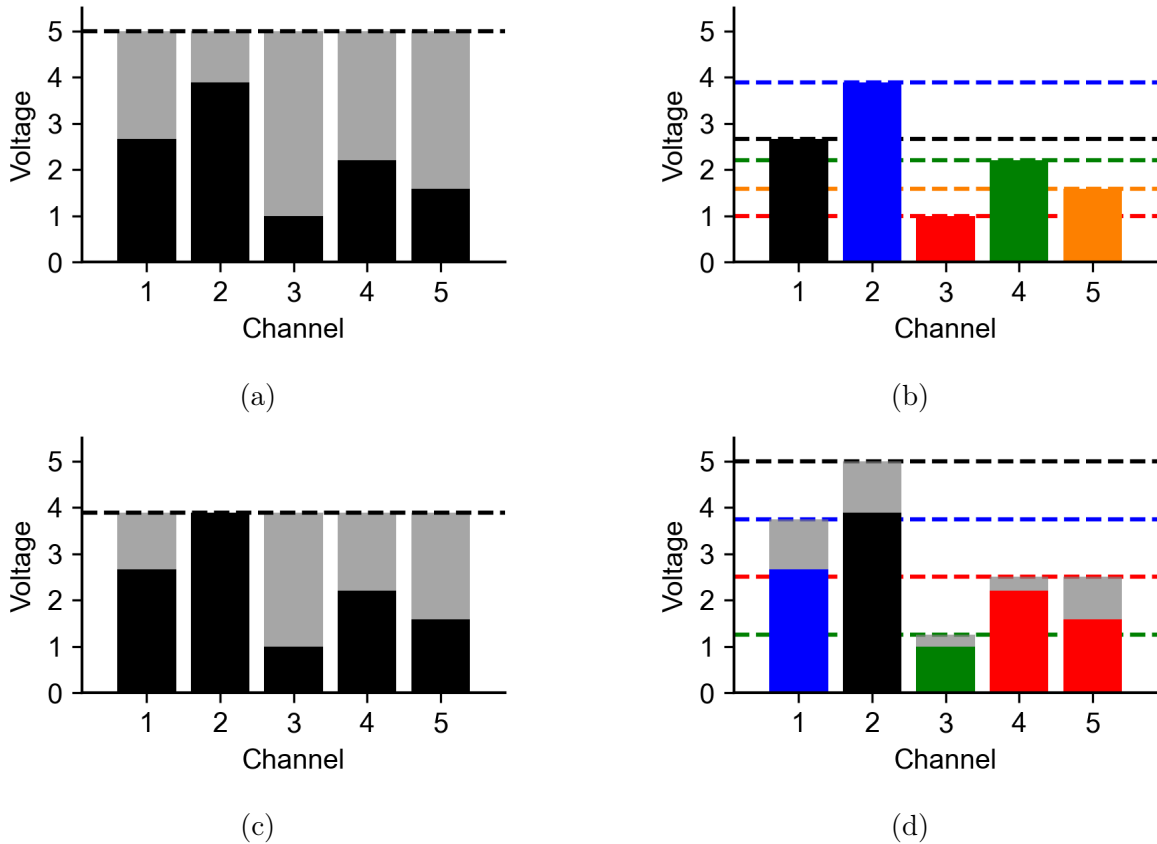


Figure 2: Illustration of the overhead losses for different voltage scaling strategies in the example of a system with five channels. Dashed, horizontal lines indicate the available voltage rails, and the colored bars the load voltage ( $V_{\text{load}}$ ) of the specific channel, where the color indicates to which voltage rail the channel is connected. Grey rectangles indicate the overhead losses. (a) In the case of a fixed voltage supply, all channels share the same voltage supply. (b) In the case of ideal supply scaling, each channel has a specific voltage supply matched to its load voltage. Thus, the overhead losses are zero. (c) With a global supply scaling strategy, a shared supply voltage is scaled to the worst-case  $V_{\text{load}}$  (channel 2 in the example), eliminating all overhead losses for that channel and reducing overhead losses in the other channels compared to the fixed voltage strategy. (d) A stepped voltage supply strategy with 4 rails. Multiple voltage rails are available, and each channel is connected to the nearest rail above its load voltage.

are detailed below. Each study has its own definitions and methods of collecting and reporting the data. Unless stated otherwise, all values are reported as (mean  $\pm$  sd).

The study by Fernández et al. [21] explored the use of a Utah Electrode Array (UEA) with 96 electrodes implanted in the visual cortex of a human patient. The authors applied stimulation trains of 50 monopolar charge-balanced cathodic-first biphasic stimuli, with a pulse width (PW) of  $170 \mu\text{s}$ , an interphase delay (IPD) of  $60 \mu\text{s}$ , and a repetition frequency of 300 Hz for the threshold procedure. A binary search procedure

was used to determine the stimulation threshold that led to a visual perception in 50 % of the trials. The magnitude of the electrode impedance was measured at 1 kHz. The current threshold for single-electrode stimulation was  $(66.8 \pm 36.5) \mu\text{A}$ , while electrode impedances of  $(47.0 \pm 4.8) \text{k}\Omega$  were recorded.

Building on similar stimulation parameters, Chen et al. [22] implanted 1024 microelectrodes (16 64-channel UEAs) in the visual cortex of two monkeys ('Monkey A' and 'Monkey L'). For both monkeys, two current thresholds are reported, one in the early stage after implantation ( $\mu_{\text{early}}$ ) and one in the late stage of the experiments ( $\mu_{\text{late}}$ ). The reported thresholds are  $\mu_{\text{early}} = (65 \pm 45) \mu\text{A}$  and  $\mu_{\text{late}} = (60 \pm 58) \mu\text{A}$  for Monkey A, and  $\mu_{\text{early}} = (19 \pm 17) \mu\text{A}$  and  $\mu_{\text{late}} = (80 \pm 71) \mu\text{A}$  for Monkey L. Additionally, we received the dataset of recorded electrode impedances from the authors. From this dataset, we obtained the impedance values (at 1 kHz) for both monkeys in the first and last experiment sessions. These values were filtered to include only electrodes with impedance below 300 k $\Omega$  for Monkey A and below 150 k $\Omega$  for Monkey L, as these electrodes were used for the current threshold measurements [22]. In Monkey A, the recorded electrode impedance was  $(144.7 \pm 72.6) \text{k}\Omega$  and  $(71.1 \pm 70.6) \text{k}\Omega$  in the early and late stages, respectively, and for Monkey L, it was  $(75.1 \pm 36.3) \text{k}\Omega$  and  $(74.9 \pm 36.4) \text{k}\Omega$ .

While Fernández and Chen focused on cortical implants, De Balthasar et al. [23] investigated epiretinal implants in six human subjects (S1-S6). Since the impedance data is only reported for subjects S4-S6, the other subjects are not included in this analysis. The array consisted of 16 (4x4) platinum electrodes in a checkerboard arrangement with alternating electrode sizes of 260  $\mu\text{m}$  and 520  $\mu\text{m}$ . The stimulation thresholds were determined using single-pulse symmetric cathodic-first pulses with a PW of 0.975 ms and an IPD of 0.975 ms. The perceptual thresholds, in this case, are defined as the current amplitude that causes a percept in 79 % of the trials. The electrode impedance was reported separately for the two sizes and are therefore treated as separate datasets in this analysis. The reported current thresholds ( $\mu_{\text{subject, size}}$ ) are:  $\mu_{\text{S4, 260}} = (233.0 \pm 20.9) \mu\text{A}$ ,  $\mu_{\text{S5, 260}} = (30.3 \pm 1.7) \mu\text{A}$ ,  $\mu_{\text{S6, 260}} = (40.9 \pm 6.1) \mu\text{A}$ ,  $\mu_{\text{S4, 520}} = (222.9 \pm 16.0) \mu\text{A}$ ,  $\mu_{\text{S5, 520}} = (26.9 \pm 1.3) \mu\text{A}$ ,  $\mu_{\text{S6, 520}} = (37.8 \pm 4.9) \mu\text{A}$ . Furthermore, the reported impedances are as follows:  $Z_{\text{S4, 260}} = (25.6 \pm 3.0) \text{k}\Omega$ ,  $Z_{\text{S5, 260}} = (40.8 \pm 1.5) \text{k}\Omega$ ,  $Z_{\text{S6, 260}} = (36.5 \pm 1.8) \text{k}\Omega$ ,  $Z_{\text{S4, 520}} = (13.6 \pm 1.1) \text{k}\Omega$ ,  $Z_{\text{S5, 520}} = (22.9 \pm 0.3) \text{k}\Omega$ ,  $Z_{\text{S6, 520}} = (18.7 \pm 0.4) \text{k}\Omega$ .

Similarly targeting retinal stimulation, Demchinsky et al. [24] implanted one human patient with the Argus II [25] retinal prosthesis. The Argus II has an epiretinal electrode array of  $6 \times 10$  platinum electrodes with a diameter of 200  $\mu\text{m}$  [25]. The parameters for stimulation thresholds and impedance measurements are not specified in this study, but the perception threshold is reported as the amplitude evoking a visual percept in 50 % of the trials. The measured perception threshold and electrode impedance after six months of implantation were  $(251 \pm 197) \mu\text{A}$  and  $(5.10 \pm 1.77) \text{k}\Omega^\ddagger$ , respectively.

Instead of targeting the central nervous system, Tan et al. [26] examined

$\ddagger$  In [24], the current and impedance values are reported in mA and  $\Omega$ , respectively in Table 2. Based on impedance and current values reported in other Argus II studies, it is assumed that this is a mistake and that these values should be  $\mu\text{A}$  and  $\text{k}\Omega$  instead.

extraneural peripheral nerve stimulation (PNS) in two human amputees. They implanted flat interface nerve electrodes (FINE) around the median and ulnar nerves in their mid-forearm and Case Western Reserve University (CWRU) electrodes around the radial nerve to produce selective sensory responses. The FINE electrode around the ulnar nerve in subject 2 did not retain good contact with the nerve and is therefore not included in the results. The stimulation pattern was a pulse train (100 Hz) of monopolar, bi-phasic, charge-balanced, cathodic-first square pulses, with a sinusoidal modulated pulse width (1 Hz) to evoke a natural, pulsing perception. Furthermore, the PW, as well as the amplitude, were stepped during the threshold process. As a result, the stimulation charge is used to report the perception threshold. However, the current amplitude is required for the power loss calculations presented in this work. To estimate the current amplitude from the reported charge thresholds, the average PW is estimated at 100  $\mu$ s, and the current threshold is calculated as  $I_{th,i} = Q_{th,i}/100\mu s$ . The resulting perception current thresholds are:  $\mu_{S1,median} = (0.96 \pm 0.43)$  mA,  $\mu_{S1,ulnar} = (0.71 \pm 0.59)$  mA,  $\mu_{S1,radial} = (0.41 \pm 0.12)$  mA,  $\mu_{S2,median} = (1.26 \pm 0.42)$  mA,  $\mu_{S2,radial} = (1.20 \pm 0.33)$  mA. To measure the electrode impedance, 0.3 mA and 50  $\mu$ s pulses at 20 and 100 Hz between pairs of electrodes within each cuff were used. The mean of eight measures of the resulting peak voltage drop between each pair of contacts was measured to calculate the impedance. The reported impedances are:  $Z_{S1,median} = (3.12 \pm 0.15)$  k $\Omega$ ,  $Z_{S1,ulnar} = (2.66 \pm 0.15)$  k $\Omega$ ,  $Z_{S1,radial} = (2.91 \pm 0.22)$  k $\Omega$ ,  $Z_{S2,median} = (2.92 \pm 0.21)$  k $\Omega$ ,  $Z_{S2,radial} = (3.09 \pm 0.19)$  k $\Omega$ .

Finally, Davis et al. [27] and George et al. [28] focused on intrafascicular PNS (iPNS) using Utah Slanted Electrode Arrays (USEA). In [27], two human amputees were implanted with a USEA of 96 electrodes in the sensory nerves in the forearm. The USEA delivers intrafascicular microstimulation, in contrast to the electrodes used in [26], which wrap around the nerve. In subject 1, the array was implanted in the median nerve, while in subject 2, it was implanted in the ulnar nerve. Biphasic, cathodic-first stimulation was used to determine the perception threshold. In most thresholding experiments, a constant frequency of 200 Hz and train duration of 0.2 s were used. The resulting perception thresholds were  $\mu_{S1} = (27.0 \pm 20.0)$   $\mu$ A,  $\mu_{S2} = (12.0 \pm 11.0)$   $\mu$ A. The electrode impedance was measured using a sinusoidal current at 1 kHz through a reference electrode. Electrodes with an impedance <500 k $\Omega$  were defined as working electrodes. The measured impedances for the working electrodes are  $Z_{S1} = (222 \pm 133)$  k $\Omega$  and  $Z_{S2} = (143 \pm 76)$  k $\Omega$ . The number of working electrodes in subject 1 rapidly dropped over the duration of the study.

A complementary study by George et al. [28] provides further insight into the long-term viability of iPNS in humans. In [28], two human amputees (S5 & S6) were chronically implanted with USEAs in their residual arm nerves to restore sensorimotor function. In both participants, one array was implanted in the median nerve and one in the ulnar nerve. The study included a third participant (S7). However, the stimulation thresholds are only reported for S5 & S6. Therefore, S7 is excluded from the analysis in this work. Contrary to the other studies, the perception threshold values in [28] are

reported in the format 'median (IQR).' The perception thresholds are reported for the first and last session, leading to a total of 8 datasets; however, since the last session in S6-ulnar contains a very limited set of electrodes, it is left out of the analysis in this work. The reported perception thresholds are as follows:  $\mu_{S5M,first} = 25 \mu\text{A}$  (17  $\mu\text{A}$ ),  $\mu_{S5U,first} = 31 \mu\text{A}$  (31  $\mu\text{A}$ ),  $\mu_{S6M,first} = 21 \mu\text{A}$  (11  $\mu\text{A}$ ),  $\mu_{S6U,first} = 36.5 \mu\text{A}$  (42.5  $\mu\text{A}$ ),  $\mu_{S5M,last} = 60 \mu\text{A}$  (40  $\mu\text{A}$ ),  $\mu_{S5U,last} = 70 \mu\text{A}$  (52.5  $\mu\text{A}$ ),  $\mu_{S6M,last} = 72.5 \mu\text{A}$  (25  $\mu\text{A}$ ). The electrode impedance data is only shown in figure format in the paper. The data behind this figure was provided to us by the authors and we used the impedance data of the first and last sessions of each participant for our analysis. The recorded impedance data is as follows:  $Z_{S5M,first} = 81.6 \text{ k}\Omega$  (99.6  $\text{k}\Omega$ ),  $Z_{S5U,first} = 77.5 \text{ k}\Omega$  (101.5  $\text{k}\Omega$ ),  $Z_{S6M,first} = 67.6 \text{ k}\Omega$  (130.6  $\text{k}\Omega$ ),  $Z_{S6U,first} = 49.0 \text{ k}\Omega$  (71.4  $\text{k}\Omega$ ),  $Z_{S5M,last} = 131.3 \text{ k}\Omega$  (163.8  $\text{k}\Omega$ ),  $Z_{S5U,last} = 178.6 \text{ k}\Omega$  (65.9  $\text{k}\Omega$ ),  $Z_{S6M,last} = 50.6 \text{ k}\Omega$  (42.8  $\text{k}\Omega$ ).

The datasets are summarized in table 1.

## 2.2. Data Analysis

The power losses at the output are the result of a mismatch between the supply voltage and the channel-specific load voltage. To compare the impact of different voltage scaling strategies, channel-specific voltage requirements need to be calculated. To that purpose, a numerical dataset with 100 000 entries per subject listed in table 1 was created. The current amplitude and electrode impedance data for these datasets were calculated using three different methods, depending on the available information. For variables reported as mean  $\pm$  sd, the dataset was assumed to follow a truncated normal distribution with the given parameters. The distribution was truncated at the reported extreme values or at the minimal step size of the parameter, ensuring no negative values were generated. For data provided as a dataset by the authors, the probability density function (PDF) of the variable was estimated using kernel density estimation. The dataset was then filled with values such that the variable followed the estimated PDF. In cases where the data was reported as the median and IQR, the distribution is also estimated to be normal. Although [28] mentions that the data is not normally distributed, the lack of additional information on the distribution led us to assume a normal distribution as a reasonable estimation. Similar to the mean  $\pm$  sd data, the dataset followed a truncated normal distribution, with the mean and standard deviation estimated from the median and IQR values, respectively.

In the resulting dataset, each entry received a random value for the current amplitude ( $I_{th}$ ) and electrode impedance ( $Z$ ), following these distributions. For simplification of the calculations, this work assumes the combined impedance of the electrode-tissue interfaces and the tissue,  $Z$ , to be real (resistive) and equal to the impedance magnitude measured at 1 kHz. The required load voltage at each entry was then calculated using the following equation

$$V_{load,i} = I_{th,i}Z_i. \quad (1)$$

Table 1: Summary of the datasets used in this work. All numerical data is presented as 'mean  $\pm$  sd,' except for [28], where it is presented as 'median (IQR).' U(S)EA = Utah (Slanted) Electrode Array, FINE = Flat Interface Nerve Electrode, V1 = Primary visual cortex, and (i)PNS = (intrafascicular) Peripheral Nerve Stimulation.

#	Source	Dataset	Electrode impedance [k $\Omega$ ]		Current threshold [ $\mu$ A]		Target	Electrodes
1	[21]	Human	47.0 $\pm$	4.8	67 $\pm$	37	V1	UEA
2	[22]	Monkey A early	144.7 $\pm$	72.6	65 $\pm$	45	V1	UEA
3	[22]	Monkey A late	71.1 $\pm$	70.6	60 $\pm$	58	V1	UEA
4	[22]	Monkey L early	75.1 $\pm$	36.3	19 $\pm$	17	V1	UEA
5	[22]	Monkey L late	74.9 $\pm$	36.4	80 $\pm$	71	V1	UEA
6	[23]	S4 260 $\mu$ m	25.6 $\pm$	0.3	233 $\pm$	21	Retina	Custom
7	[23]	S5 260 $\mu$ m	40.8 $\pm$	1.5	30 $\pm$	2	Retina	Custom
8	[23]	S6 260 $\mu$ m	36.5 $\pm$	1.8	41 $\pm$	6	Retina	Custom
9	[23]	S4 520 $\mu$ m	13.6 $\pm$	1.1	222 $\pm$	16	Retina	Custom
10	[23]	S5 520 $\mu$ m	22.9 $\pm$	0.3	27 $\pm$	1	Retina	Custom
11	[23]	S6 520 $\mu$ m	18.7 $\pm$	0.4	38 $\pm$	5	Retina	Custom
12	[24]	Human	5.1 $\pm$	1.8	251 $\pm$	197	Retina	Argus II
13	[26]	S1 median	3.1 $\pm$	0.2	955 $\pm$	425	PNS	FINE
14	[26]	S1 ulnar	2.7 $\pm$	0.2	707 $\pm$	592	PNS	FINE
15	[26]	S1 radial	2.9 $\pm$	0.2	407 $\pm$	124	PNS	FINE
16	[26]	S2 median	2.9 $\pm$	0.2	1260 $\pm$	415	PNS	FINE
17	[26]	S1 radial	3.1 $\pm$	0.2	1200 $\pm$	325	PNS	FINE
18	[27]	S1 median	222 $\pm$ 133		27 $\pm$	20	iPNS	USEA
19	[27]	S2 ulnar	143 $\pm$ 76		12 $\pm$	11	iPNS	USEA
20	[28]	S5-M first	81.6 (99.6)		25 (17)		iPNS	USEA
21	[28]	S5-U first	77.5 (101.5)		31 (31)		iPNS	USEA
22	[28]	S6-M first	67.6 (130.6)		21 (11)		iPNS	USEA
23	[28]	S6-U first	49.0 (71.4)		37 (43)		iPNS	USEA
24	[28]	S5-M last	131.3 (163.8)		60 (40)		iPNS	USEA
25	[28]	S5-U last	178.6 (65.9)		70 (53)		iPNS	USEA
26	[28]	S6-M last	50.6 (42.8)		73 (25)		iPNS	USEA

Using this dataset, the power losses of different voltage scaling strategies were calculated as described in section 2.3. The resulting data is available at [29].

### 2.3. Calculating Power Losses

In the ideal case, when the voltage supply tracks the load voltage accurately for each channel (figure 2b), all the power at the output is delivered to the load. Using the



current and impedance information, the load power can be calculated as:

$$P_{\text{load},i} = I_{\text{th},i}^2 Z_i. \quad (2)$$

This will be used as a reference to calculate the efficiencies of all non-ideal cases using:

$$\eta = \frac{P_{\text{load},i}}{P_{\text{load},i} + P_{\text{loss},i}}. \quad (3)$$

In the case of a fixed voltage supply (figure 2a), the power losses at each channel can be calculated using:

$$P_{\text{loss,fixed},i} = (V_{\text{fixed}} - V_{\text{load},i})I_{\text{th},i}, \quad (4)$$

where  $V_{\text{fixed}}$  is the same for all channels. Different scenarios for the magnitude of  $V_{\text{fixed}}$  are considered. When designing a system to deliver the stimulation from a fixed voltage supply, different considerations could lead to the choice of  $V_{\text{fixed}}$ . First of all, one can consider the maximum voltage for each subject separately to calculate the losses. This will be referred to as a subject-specific voltage supply. However, this assumes that the voltage distribution for a subject would be known before implementing the system, which is usually not the case. Rather, the voltage supply is likely to be designed for the application specifications. In this case,  $V_{\text{fixed}}$  can be based on grouping all data with the same target (in table 1) together. In this work, this scenario will be referred to as an application-specific supply. Furthermore, a reasonable design consideration is the trade-off between yield and efficiency. Here, yield is defined as the percentage of the total number of available channels that can be stimulated. If  $V_{\text{fixed}} < \max(V_{\text{load,target}})$ , not all channels can be stimulated, resulting in a lower yield, but the overall system efficiency will improve. For the application-specific calculations in this work, a yield of 75% is chosen. In other words,  $V_{\text{app}}$  is equal to the third quantile ( $Q_3$ ) of  $V_{\text{load,target}}$ . Similarly, the subject-specific voltage,  $V_{\text{sub}}$  is equal to  $Q_3$  of  $V_{\text{load,subject}}$ . Note that a yield of 75% might be considered low for some applications and that higher yields are desirable. This will favor the more flexible scaling strategies as the variability in load voltages increases. Finally, the technology used to design the stimulator circuit will also influence the choice of  $V_{\text{fixed}}$  as some values (e.g., 3.3 V, 5 V, 10 V) are common practice for given technologies. This consideration is not included in the analyses presented in this work, but the analysis could easily be repeated with these constraints.

The first supply scaling strategy considered in this work is the use of a globally scaled supply voltage (figure 2c). In this case, the global supply would have to accommodate for the worst-case channel that is being stimulated. To calculate the losses for this scenario, a set of  $M$  channels is sampled from the dataset, and the losses are calculated as:

$$P_{\text{loss,global},i} = (\max(V_{\text{load},j}) - V_{\text{load},i})I_{\text{th},i}, j \in M, \quad (5)$$

where the size of  $M$  is chosen based on the application. For intracortical visual prostheses, current efforts are aimed at developing systems with more than 1000 channels to provide high-resolution visual information that could restore useful vision [1]. In retinal prostheses, it has been estimated that 625 channels would be sufficient for useful

vision [30]. However, using smaller and more electrodes could improve the field of view and efficacy of the implant [31]. In the case of PNS applications, the channel requirements are generally much lower. For intrafascicular interfaces, such as those using the USEA, one or two arrays, each with 100 channels, can provide sufficient information for neuroprosthetic applications [28]. This suggests that a total channel count of approximately 200 may be adequate for many tasks. On the other hand, extraneural electrodes, such as the FINE, offer much lower resolution, with individual electrodes typically containing only 8 channels. Therefore, a system utilizing two FINE electrodes would have only 16 channels in total [26]. Additionally, only a subset of the total channel will be active at the same time. For this analysis, it is assumed that only 20% of the channels will be active simultaneously. As a result, the sample size,  $M$ , for the different applications is 200, 125, 40, and 4 for V1, Retinal, iPNS, and extraneural PNS, respectively.

The other supply scaling strategy is the use of a stepped supply voltage (figure 2d). In this case,  $N$  voltage steps are created, and each channel is connected to the nearest available step above the load voltage. Thus, the power losses can be calculated as:

$$P_{\text{loss,stepped},i} = (V_{\text{step},i} - V_{\text{load},i})I_{\text{th},i}, \quad (6)$$

where  $V_{\text{step},i}$  is the nearest available voltage rail above  $V_{\text{load},i}$ . The available supply rails depend on the number of steps chosen. The application-specific voltage supply is used as the maximum voltage, and the steps are uniformly distributed. As an example, in the case of  $V_{\text{app}} = 5\text{V}$  and  $N = 4$ , the available voltage steps will be:  $V_{\text{step}} = \{1.25, 2.5, 3.75, 5\}\text{V}$ .

### 3. Results

#### 3.1. Voltage and load power distributions

The calculated load voltage distributions (equation (1)) are shown in figure 3a. The resulting load voltage for the different applications are 3.5 V (5.3 V) (median (IQR)), 3.9 V (6.2 V), 1.3 V (2.2 V), and 2.8 V (2.4 V) for iPNS, V1, Retina, and PNS, respectively. These results suggest that PNS and Retina stimulation operate at relatively lower voltages compared to iPNS and V1, reflecting varying requirements across applications.

The corresponding load power distributions (equation (2)) are presented in figure 3b. The resulting values are as follows: 117  $\mu\text{W}$  (308  $\mu\text{W}$ ) for iPNS, 240  $\mu\text{W}$  (639  $\mu\text{W}$ ) for V1, 55  $\mu\text{W}$  (652  $\mu\text{W}$ ) for Retina, and 2.5 mW (4.2 mW) for PNS. These results show that the median load power per channel is highly application-dependent, spanning more than one order of magnitude between Retinal and PNS stimulation.

To further explore inter-subject differences, the load voltage and power distributions of all subjects are compared in figure 4. This figure highlights the differences between applications. For Retinal stimulation, the load power spans a wide range on the application level, while the range within each subject is small. On the other hand,

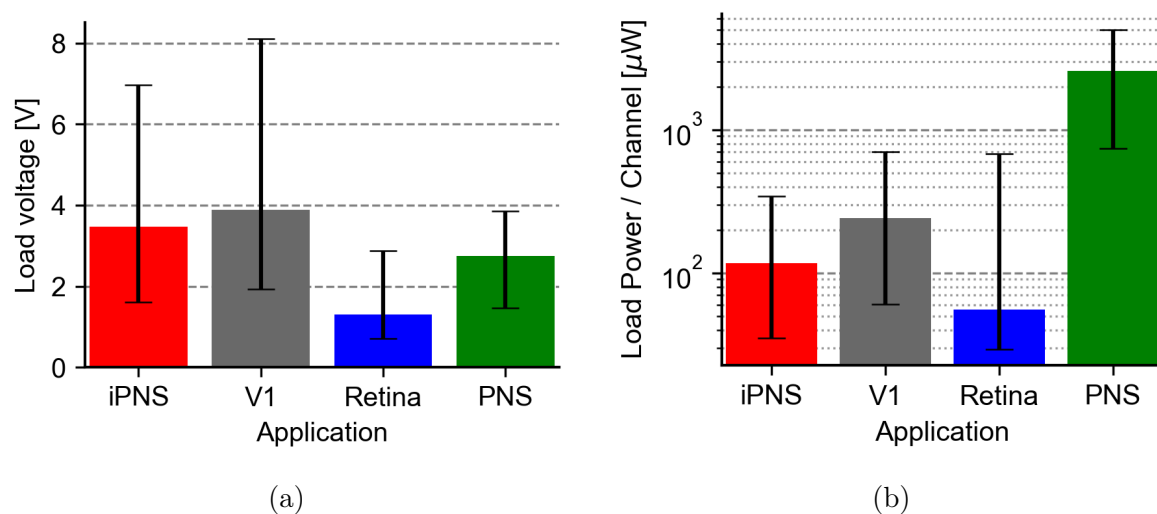


Figure 3: Load (a) voltage and (b) power per channel distributions grouped by application. The bars indicate the median value, with error bars representing the IQR.

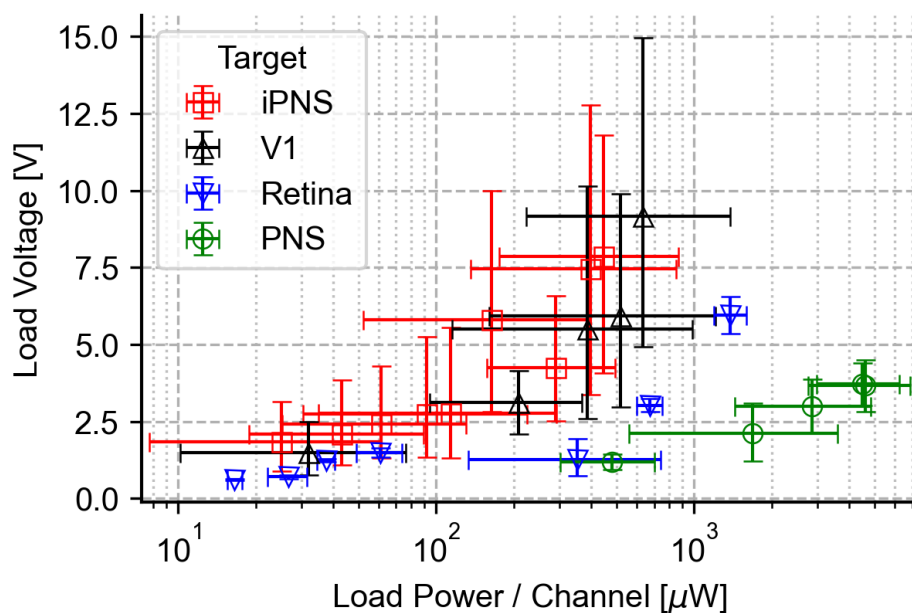


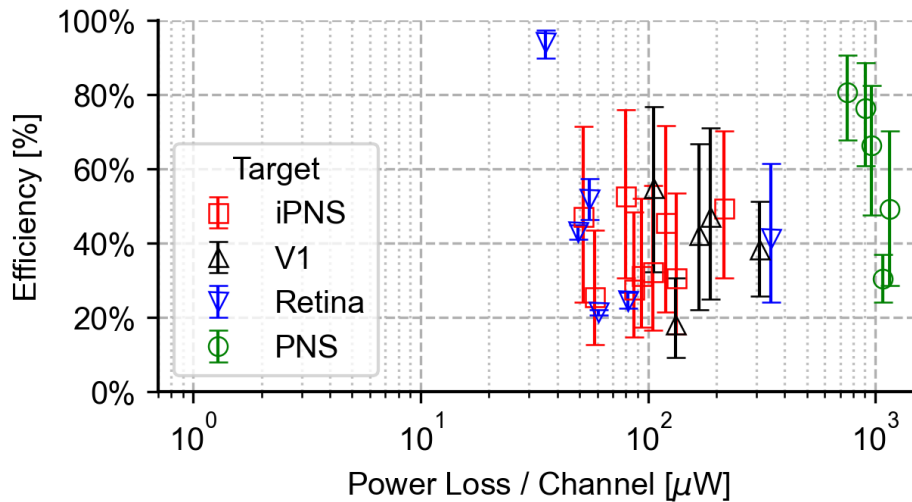
Figure 4: Load voltage and power distributions of the individual datasets. Markers indicate the median value and error bars the IQR.

both iPNS and V1 stimulation show wide ranges both on the application level and on the subject level.

The application-specific voltage supplies derived from these results, used in subsequent power loss calculations, are listed in table 2.

Table 2: Application-specific voltage supply used for the power loss calculations.

Application	$V_{\text{app}}$ [V]
iPNS	7.0
V1	8.1
Retina	2.9
PNS	3.9

Figure 5: Calculated power loss per channel (Median & IQR) and the corresponding efficiencies for an application-specific voltage supply ( $V_{\text{app}}$ ).

### 3.2. Losses with fixed voltage supply

The power losses per channel for a conventional fixed voltage supply were calculated for two scenarios: application-specific and subject-specific power supplies. For the application-specific case, figure 5 shows that most subjects exhibit efficiencies below 60%, with power losses typically in the range of 100  $\mu\text{W}$  per channel. However, PNS subjects display higher efficiencies despite experiencing greater power losses in the order of 1 mW per channel. This emphasizes that even though efficiencies may be high, it could still be worth improving to save significant power.

When using subject-specific voltage supplies (figure 6), the general trend is an improvement in efficiency and a reduction in power loss per channel. Retina stimulation, in particular, achieves consistently high efficiencies, which is due to the small inter-subject variance shown in figure 4.

### 3.3. Losses for global supply scaling

The efficiencies and power loss per channel for global supply scaling are compared to fixed voltage supplies in figure 7. Compared to  $V_{\text{sub}}$ , this type of voltage scaling does

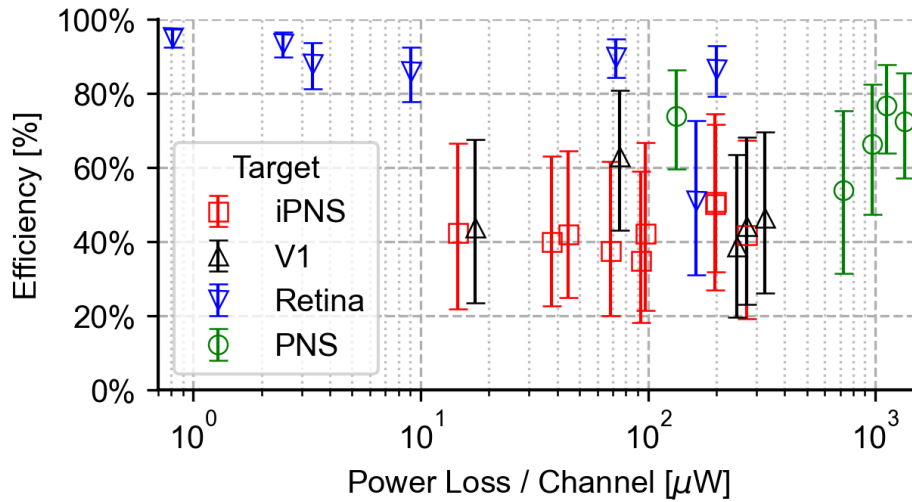


Figure 6: Calculated power loss per channel (Median & IQR) and the corresponding efficiencies for a subject-specific voltage supply ( $V_{\text{sub}}$ ).

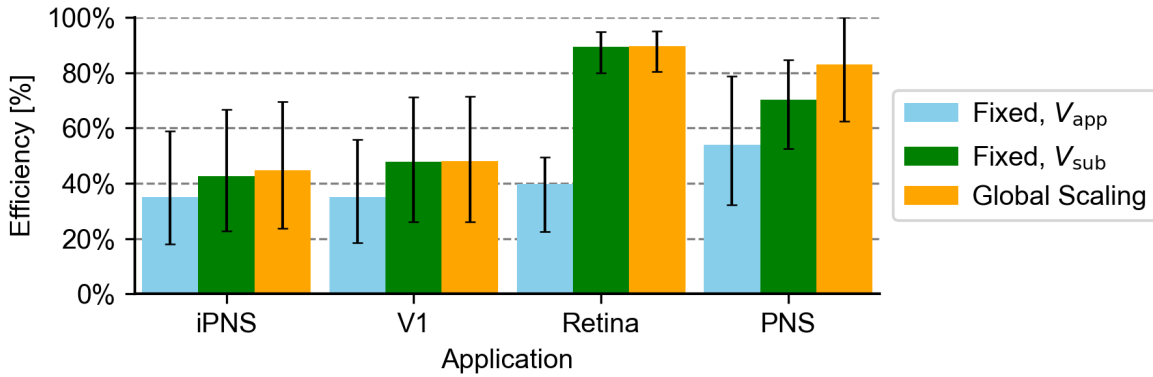
not improve the efficiency in high-channel-count applications (iPNS, V1, Retina) due to the variation in voltage requirements and the fact that the supply has to accommodate the worst case. However, in low-channel-count applications like PNS, the approach can reduce power losses substantially. For PNS, the median power loss per channel is reduced from  $791 \mu\text{W}$  to  $243 \mu\text{W}$ , while the median efficiency is increased from  $70.2\%$  to  $81.5\%$ . These results highlight that global scaling is most effective when the channel count is low and the variability in voltage requirements is minimal.

#### 3.4. Losses for a stepped supply

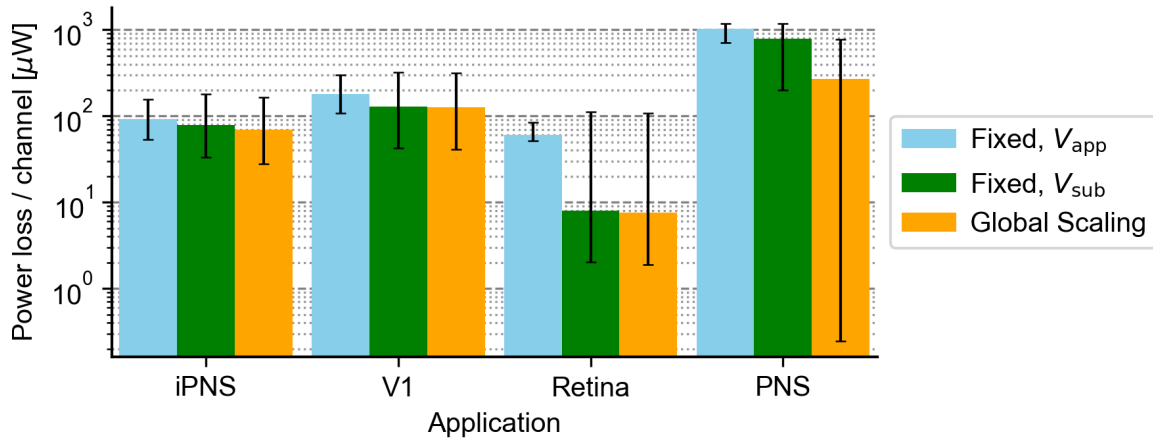
For the stepped supply strategy, the power loss reduction and efficiency improvements are calculated for uniformly distributed supplies of 1 (fixed), 2, 4, and 8 voltage rails. This strategy demonstrates efficiency improvements across all applications (figure 8), with efficiencies exceeding  $85\%$  when using eight voltage rails. Compared to the fixed voltage supply, this yields an increase in efficiency of  $67\%$  (PNS) to  $146\%$  (iPNS). However, the incremental benefit of adding more rails diminishes with each step. Nonetheless, the flexibility to tune each channel specifically makes this strategy broadly applicable.

#### 3.5. Comparison of scaling strategies

The comparative performance of all strategies is summarized in figure 9. It is shown that all scaling strategies lead to considerable improvements compared to the conventional fixed supply case. There is not one strategy that outperforms the rest for all applications, suggesting that tailoring the strategy to the specific application will improve its benefits. Furthermore, in some cases, one strategy outperforms the others, but other factors, such



(a)

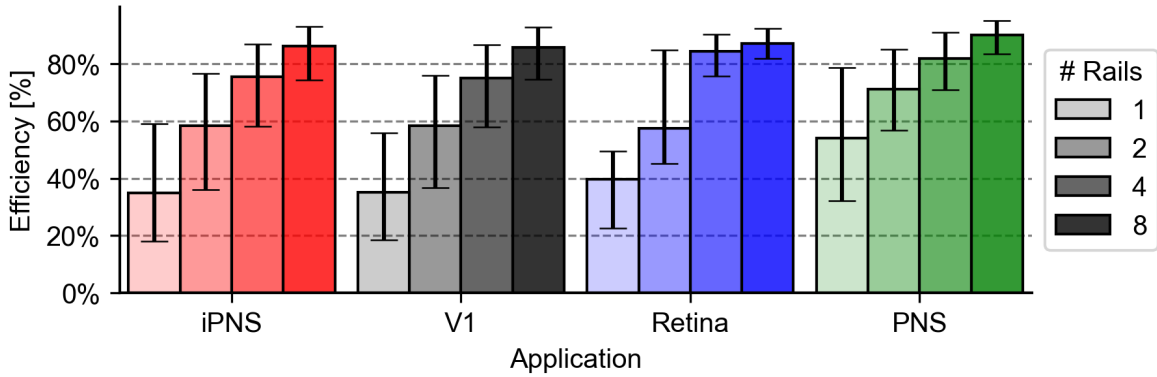


(b)

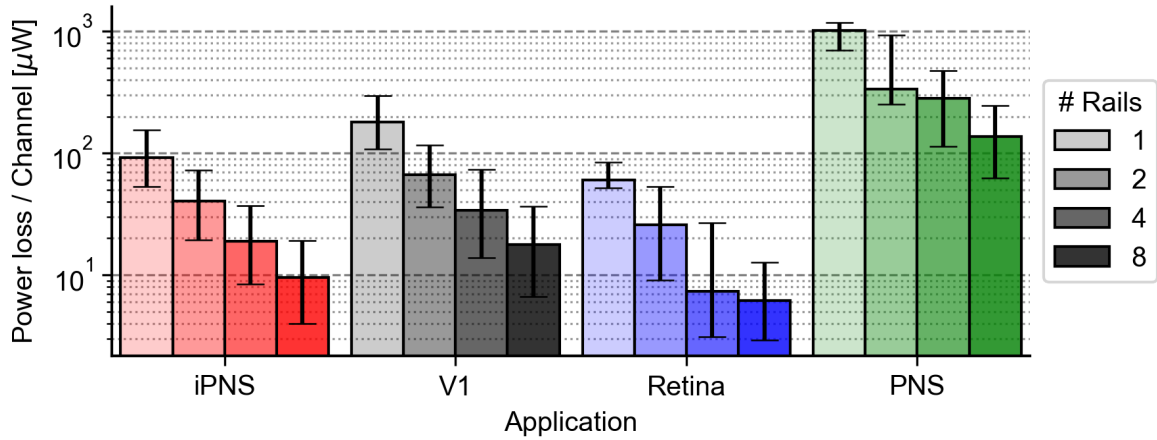
Figure 7: The effect of a global supply scaling strategy on the (a) efficiency and (b) power loss per channel for the different applications. The bars indicate the median value, with error bars representing the IQR.

as design complexity, may still favor another strategy. Considerations regarding circuit implementations will be discussed in section 4.1.

Even though the scaling strategies show substantial improvements in efficiency, there is still room for further reduction of the power losses. For each application, the total power loss can be calculated by multiplying the number of channels in that application with the channel losses presented in figure 9b. For the best scaling strategy in each application, this results in a total system power loss of 382  $\mu\text{W}$  (605  $\mu\text{W}$ ), 3.5 mW (6.0 mW), 766  $\mu\text{W}$  (1228  $\mu\text{W}$ ), 551  $\mu\text{W}$  (738  $\mu\text{W}$ ) for iPNS, V1, Retina, and PNS, respectively.



(a)



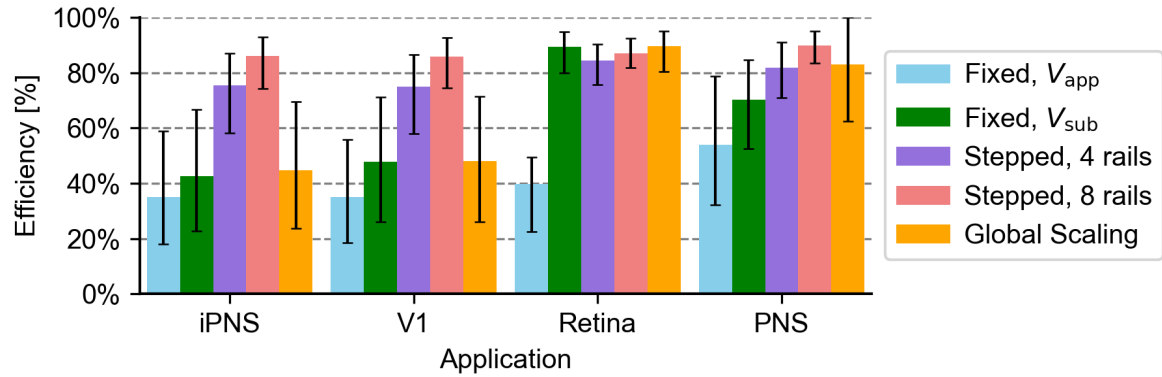
(b)

Figure 8: Effect of a stepped-voltage supply strategy from an application-specific supply on the (a) efficiency and (b) power loss per channel in the different applications. The bars indicate the median value, with error bars representing the IQR.

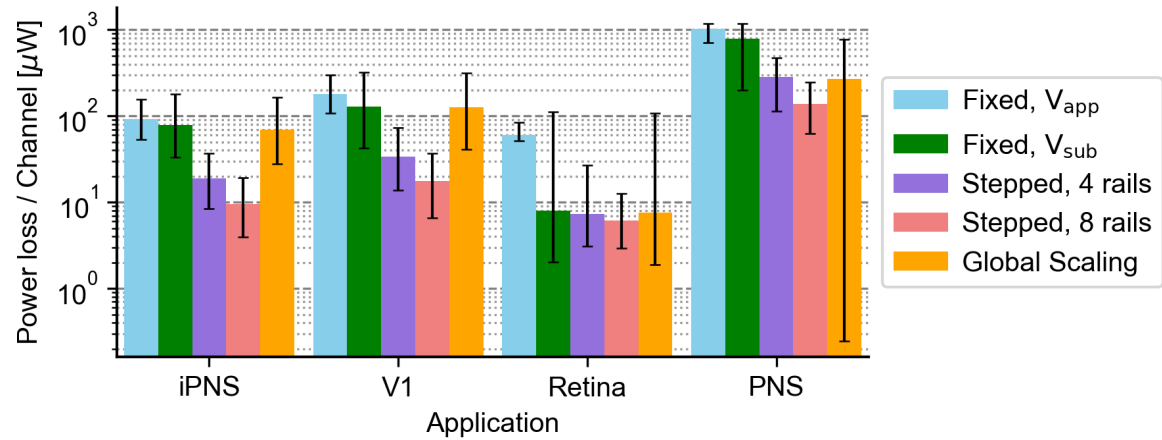
## 4. Discussion

### 4.1. Circuit Design Considerations

The power losses were calculated for two types of fixed supplies. Both of these calculations assume that information on the voltage distribution of the application or subject is known when designing the system. In reality, most systems will be designed adhering to common voltage levels depending on the technology used for the circuit design. However, all datasets showed that a subject-specific power supply could lead to substantial improvements in output efficiency. These results indicate that developing stimulator systems with a programmable supply voltage would be worthwhile. When combined with voltage or impedance measurement functionalities, the subject-specific voltage distribution can be measured, and the supply voltage can be adjusted accordingly.



(a)



(b)

Figure 9: Comparison of the impact of the scaling strategies on the (a) efficiency and (b) power loss per channel in the different applications. The bars indicate the median value, with error bars representing the IQR.

When the channel count of an application is high, it was shown that the global scaling strategy does not add many benefits compared to the subject-specific fixed supply voltage. However, in low channel-count applications, the strategy can further improve efficiency. Implementing a global scaling strategy adds circuit complexity to each channel, as it requires a voltage compliance monitor to determine what the supply voltage should be [32–34]. On the other hand, the yield could be higher as the supply voltage can temporarily increase when needed, which could accommodate more channels than a reduced fixed supply.

A stepped voltage supply outperformed the other strategies for applications with high intrasubject variability (e.g., V1 and iPNS). Rationally, increasing the number of voltage steps reduces the losses. However, it comes with increased complexity in the electronics at the system and channel level. At a system level, increasing the number of voltage rails in the multi-output supply increases its complexity. Each voltage rail requires a storage capacitor to make it possible to deliver power, which can increase



the area requirements. Furthermore, all voltage rails need to be distributed towards all channels. In high-channel-count applications, this can become a bottleneck for increasing the number of rails. At the channel level, a voltage rail selector needs to be implemented. With more rails available, the selector circuit increases in size and complexity. Since the area requirements are highly technology-dependent, it is difficult to estimate the cost of each implementation. However, when the technology parameters are known, the presented analysis can serve to make a trade-off between efficiency and complexity.

Finally, for each scaling strategy, additional power losses should be considered. Additional losses could come from reduced rectifier efficiency, extra conversion steps, and additional control and compliance circuitry. In this respect, the power per channel for the application is an important weighting factor. When the load power per channel is low, overhead losses in the channel can quickly diminish the efficiency improvements gained by the scaling strategy. Sharing resources among multiple channels helps to reduce the impact on the efficiency. When the power per channel is high, the design requirements for the scaling circuitry are easier in terms of power consumption since overhead losses are less important.

#### *4.2. Temporal changes*

The datasets used in this study all represent a static set of parameters. However, impedance and stimulation thresholds are known to change over time [12, 22, 28]. Therefore, the voltage requirements of the channels and resulting losses will change accordingly. Flexibility in the voltage supply helps to accommodate changes and reduce power losses over time. In the long term, this will lead to the best power efficiency during the lifetime of the implant.

#### *4.3. Limitations of current work*

The analysis presented here is based on previously published data. Here, we reflect on the limitations of the assumptions necessary to perform the analysis.

First, for most datasets, the distribution of the parameters was assumed to be (truncated) Gaussian. This assumption was made due to a lack of information; in reality, the distributions could have been different. As described in section 2.2, an extended analysis was performed when more information regarding the data distribution was available.

Furthermore, the impedance and current data are assumed to be uncorrelated. While [23] found a negative correlation between the two parameters, the other studies did not report the correlation. Variations in electrode impedance are caused by many factors, which might change the correlation between impedance and threshold values. In [23], the critical factor influencing impedance and threshold was the distance between the electrode and the retina. If the correlation of these parameters is known for a specific application, it could be added to the generation of the dataset to evaluate its effects.

Additionally, the size of the electrodes used in the retina data is relatively big. The development trend in retinal implants is to reduce the size of the electrodes to bring them closer to the retina and achieve higher electrode count and density [35, 36]. However, no data could be found on human subjects for the smaller electrodes, where both impedance measurements and perception thresholds were reported. Generally speaking, reducing the electrode size will increase the impedance, and bringing the electrodes closer to the cells will reduce stimulation thresholds [23].

Last, the electrode impedance is more complex than the 1 kHz value used in this work to calculate the losses. A more realistic model includes the capacitive effects of the electrode-tissue interface (ETI). This capacitive component affects the load voltage and will change the load power. The extent of this effect depends on the ratio between the resistive and capacitive components of the load impedance, as well as the delivered charge [37]. Therefore, it depends on the type of electrodes used. Ideally, the capacitance of stimulation electrodes should be large to prevent depolarization of the ETI, which can lead to non-reversible charge transfer [10]. Specifically, in microelectrodes, the resistive component is typically dominant, and the effect of the capacitance on the power calculations will be minimal.

## **5. Conclusion**

This work presents a novel methodology for analyzing power losses and evaluating the efficacy of minimization strategies in multichannel electrical stimulation systems, integrating both electrophysiological and electronic perspectives. Traditional stimulator systems are often designed for fixed load conditions, overlooking the significant impact of inter-channel variability in electrode impedance and current thresholds. By incorporating these variabilities into the analysis, the proposed method enables more elaborate assessments of the power efficiency across scaling strategies and applications. Furthermore, the method serves as a tool for guiding the design of new systems, providing insights into which scaling strategy offers the best performance under specific conditions.

The methodology was applied to experimental data from various multichannel applications. The stepped voltage strategy showed an efficiency improvement of 67% to 146%, proving to be most effective for applications with many channels and large inter-channel variability. Conversely, global voltage scaling emerged as a viable option for applications with lower channel counts or minimal inter-channel variability. The results confirm that there is no universal best approach across the scaling strategies. Instead, tailored scaling strategies will lead to the best power efficiency for each application. Furthermore, it is important to consider additional design complexity and power losses when deciding on the best strategy for a specific application. These factors are technology- and application-dependent and can not be generalized. When designing a system for new multichannel applications, the presented analysis can guide the design trade-offs to choose the best approach.

Finally, the calculated total system power losses show that there is still room for improvement in more advanced methods to increase power efficiency even further. By developing novel systems that support voltage scaling techniques, power efficiency can be enhanced, allowing for increasing the number of stimulation channels in next-generation, large-scale neural interfaces.

## Acknowledgments

We want to thank the authors of the original datasets, specifically Xing Chen and Jacob George, for sharing additional data and insights. This research was supported by NWO, the Dutch Research Council, under project number 17619 ‘INTENSE.’

## References

- [1] Eduardo Fernández, Arantxa Alfaro, and Pablo González-López. Toward Long-Term Communication With the Brain in the Blind by Intracortical Stimulation: Challenges and Future Prospects. *Frontiers in Neuroscience*, 14(August), 8 2020.
- [2] Elon Musk. An integrated brain-machine interface platform with thousands of channels. *Journal of Medical Internet Research*, 21(10), 10 2019.
- [3] Taesung Jung, Nanyu Zeng, Jason D Fabbri, Guy Eichler, Zhe Li, Konstantin Willeke, Katie E Wingel, Agrita Dubey, Rizwan Huq, Mohit Sharma, Yaoming Hu, Girish Ramakrishnan, Kevin Tien, Paolo Mantovani, Abhinav Parihar, Heyu Yin, Alexander Misdorp, Ilke Uguz, Tori Shinn, Gabrielle J Rodriguez, Cate Nealley, Ian Gonzales, Michael Roukes, Jeffrey Knecht, Daniel Yoshor, Peter Canoll, Eleonora Spinazzi, Luca P Carloni, Bijan Pesaran, Saumil Patel, Brett Youngerman, R James Cotton, Andreas Tolia, and Kenneth L Shepard. Stable, chronic in-vivo recordings from a fully wireless subdural-contained 65,536-electrode brain-computer interface device. *BioRxiv*, 2024.
- [4] Yan Liu, Alessandro Urso, Ronaldo Martins, Tiago Costa, Virgilio Valente, Vasiliki Giagka, Wouter A Serdijn, Timothy G Constandinou, and Timothy Denison. Bidirectional Bioelectronic Interfaces. *IEEE solid state circuits magazine*, 12(2):30–46, 2020.
- [5] Sofia Drakopoulou, Francesc Varkevisser, Linta Sohail, Masoumeh Aqamolaei, Tiago L. Costa, and George D. Spyropoulos. Hybrid neuroelectronics: towards a solution-centric way of thinking about complex problems in neurostimulation tools. *Frontiers in Electronics*, 4, 9 2023.
- [6] Tom P. G. van Nunen, Rob M. C. Mestrom, and Hubregt J. Visser. Wireless Power Transfer to Biomedical Implants Using a Class-E Inverter and a Class-DE Rectifier. *IEEE Journal of Electromagnetics, RF and Microwaves in Medicine and Biology*, pages 1–8, 2023.

- [7] IEEE International Committee on Electromagnetic Safety (SCC39). IEEE Std C95.1<sup>TM</sup>-2005: IEEE Standard for Safety Levels with Respect to Human Exposure to Radio Frequency Electromagnetic Fields, 3 kHz to 300 GHz. Technical report, Institute of Electrical and Electronics Engineers (IEEE), New York, NY, USA, 2005. ISBN: 978-0-7381-4772-3.
- [8] International Organization for Standardization. ISO 14708-3:2017: Implants for surgery — Active implantable medical devices — Part 3: Implantable neurostimulators. Technical Report ISO 14708-3:2017, International Organization for Standardization, Geneva, Switzerland, 2017. Safety and performance requirements for implantable neurostimulators.
- [9] Rohollah Shirafkan and Omid Shoaie. Current-Based Neurostimulation Circuit and System Techniques. In *Handbook of Biochips*, pages 445–469. Springer New York, New York, NY, 2022.
- [10] Daniel R. Merrill, Marom Bikson, and John G.R. Jefferys. Electrical stimulation of excitable tissue: design of efficacious and safe protocols. *Journal of Neuroscience Methods*, 141(2):171–198, 2 2005.
- [11] Francesc Varkevisser, Tiago L. Costa, and Wouter A. Serdijn. Multichannel current-mode stimulator with channel-specific regulated power supply. In *2023 IEEE Biomedical Circuits and Systems Conference (BioCAS)*, pages 1–5. IEEE, 10 2023.
- [12] T. S. Davis, R. A. Parker, P. A. House, E. Bagley, S. Wendelken, R. A. Normann, and B. Greger. Spatial and temporal characteristics of V1 microstimulation during chronic implantation of a microelectrode array in a behaving macaque. *Journal of Neural Engineering*, 9(6):065003, 12 2012.
- [13] S. K. Arfin and R. Sarpeshkar. An Energy-Efficient, Adiabatic Electrode Stimulator With Inductive Energy Recycling and Feedback Current Regulation. *IEEE Transactions on Biomedical Circuits and Systems*, 6(1):1–14, 2 2012.
- [14] Shawn K. Kelly. Adiabatic Electrode Stimulator. In *Handbook of Biochips*, pages 1157–1183. Springer New York, New York, NY, 2022.
- [15] Zhicong Luo, Ming-Dou Ker, Tzu-Yi Yang, and Wan-Hsueh Cheng. A Digitally Dynamic Power Supply Technique for 16-Channel 12 V-Tolerant Stimulator Realized in a 0.18- $\mu\text{m}$  1.8-V/3.3-V Low-Voltage CMOS Process. *IEEE Transactions on Biomedical Circuits and Systems*, 11(5):1087–1096, 10 2017.
- [16] Ian Williams and Timothy G. Constandinou. An Energy-Efficient, Dynamic Voltage Scaling Neural Stimulator for a Proprioceptive Prosthesis. *IEEE Transactions on Biomedical Circuits and Systems*, 7(2):129–139, 4 2013.
- [17] Kyeongho Eom, Minju Park, Han Sol Lee, Seung Beom Ku, Namju Kim, Seongkwang Cha, Yong Sook Goo, Sohee Kim, Seong Woo Kim, and Hyung Min Lee. A Low-Stimulus-Scattering Pixel-Sharing Sub-Retinal Prosthesis SoC With Time-Based Photodiode Sensing and Per-Pixel Dynamic Voltage Scaling. *IEEE Journal of Solid-State Circuits*, 58(11):2976–2989, 11 2023.

- [18] Kim Hoang Nguyen, Woojin Ahn, Minkyu Je, Quyet Nguyen, Quynh Trang Nguyen, Thanh Tung Vu, and Loan Pham-Nguyen. A Neural Stimulator IC with Dynamic Voltage Scaling Supply and Energy Recycling for Cochlear Implant in Standard 180nm CMOS Process. In *Proceedings - International SoC Design Conference 2023, ISODC 2023*, pages 35–36. Institute of Electrical and Electronics Engineers Inc., 2023.
- [19] Amin Rashidi, Niloofar Yazdani, and Amir M. Sodagar. Fully implantable, multi-channel microstimulator with tracking supply ribbon, multi-output charge pump and energy recovery. *IET Circuits, Devices & Systems*, 15(2):104–120, 3 2021.
- [20] Hyun-Su Lee, Kyeongho Eom, and Hyung-Min Lee. 27.3 A 90.8%-Efficiency SIMO Resonant Regulating Rectifier Generating 3 Outputs in a Half Cycle with Distributed Multi-Phase Control for Wirelessly-Powered Implantable Devices. In *2024 IEEE International Solid-State Circuits Conference (ISSCC)*, pages 448–450. IEEE, 2 2024.
- [21] Eduardo Fernández, Arantxa Alfaro, Cristina Soto-Sánchez, Pablo Gonzalez-Lopez, Antonio M. Lozano, Sebastian Peña, Maria Dolores Grima, Alfonso Rodil, Bernardeta Gómez, Xing Chen, Pieter R. Roelfsema, John D. Rolston, Tyler S. Davis, and Richard A. Normann. Visual percepts evoked with an intracortical 96-channel microelectrode array inserted in human occipital cortex. *Journal of Clinical Investigation*, 131(23), 12 2021.
- [22] Xing Chen, Feng Wang, Roxana Kooijmans, Peter Christiaan Klink, Christian Boehler, Maria Asplund, and Pieter Roelf Roelfsema. Chronic stability of a neuroprosthesis comprising multiple adjacent Utah arrays in monkeys. *Journal of Neural Engineering*, 20(3), 6 2023.
- [23] Chloé De Balthasar, Sweta Patel, Arup Roy, Ricardo Freda, Scott Greenwald, Alan Horsager, Manjunatha Mahadevappa, Douglas Yanai, Matthew J. McMahan, Mark S. Humayun, Robert J. Greenberg, James D. Weiland, and Ione Fine. Factors affecting perceptual thresholds in epiretinal prostheses. *Investigative Ophthalmology and Visual Science*, 49(6):2303–2314, 6 2008.
- [24] Andrey M. Demchinsky, Timur B. Shaimov, Daria N. Goranskaya, Irina V. Moiseeva, Daniil I. Kuznetsov, Denis S. Kuleshov, and Dmitry V. Polikanov. The first deaf-blind patient in Russia with Argus II retinal prosthesis system: What he sees and why. *Journal of Neural Engineering*, 16(2), 2019.
- [25] Yvonne Hsu-Lin Luo and Lyndon da Cruz. The Argus® II Retinal Prosthesis System. *Progress in Retinal and Eye Research*, 50:89–107, 1 2016.
- [26] Daniel W Tan, Matthew A Schiefer, Michael W Keith, J Robert Anderson, and Dustin J Tyler. Stability and selectivity of a chronic, multi-contact cuff electrode for sensory stimulation in human amputees. *Journal of Neural Engineering*, 12(2):026002, 4 2015.
- [27] T. S. Davis, H. A.C. Wark, D. T. Hutchinson, D. J. Warren, K. O’Neill, T. Scheinblum, G. A. Clark, R. A. Normann, and B. Greger. Restoring motor

- control and sensory feedback in people with upper extremity amputations using arrays of 96 microelectrodes implanted in the median and ulnar nerves. *Journal of Neural Engineering*, 13(3), 3 2016.
- [28] Jacob A. George, David M. Page, Tyler S. Davis, Christopher C. Duncan, Douglas T. Hutchinson, Loren W. Rieth, and Gregory A. Clark. Long-term performance of Utah slanted electrode arrays and intramuscular electromyographic leads implanted chronically in human arm nerves and muscles. *Journal of Neural Engineering*, 17(5), 10 2020.
- [29] Francesc Varkevisser, Wouter A. Serdijn, and Tiago L. Costa. Data underlying manuscript: Analysis of power losses and the efficacy of power minimization strategies in multichannel electrical stimulation systems. <https://doi.org/10.4121/b8098fe4-3f33-4691-9e55-54bf2cc255c3>, 2025.
- [30] Eyal Margalit, Mauricio Maia, James D Weiland, Robert J Greenberg, Gildo Y Fujii, Gustavo Torres, Duke V Piyathaisere, Thomas M O’Hearn, Wentai Liu, Gianluca Lazzi, Gislin Dagnelie, Dean A Scribner, Eugene de Juan, and Mark S Humayun. Retinal Prosthesis for the Blind. *Survey of Ophthalmology*, 47(4):335–356, 7 2002.
- [31] Daniel Palanker, Alexander Vankov, Phil Huie, and Stephen Baccus. Design of a high-resolution optoelectronic retinal prosthesis. *Journal of Neural Engineering*, 2(1):S105–S120, 3 2005.
- [32] Maurits Ortmanns, André Rocke, Marcus Gehrke, and Hans-Jürgen Tiedtke. A 232-Channel Epiretinal Stimulator ASIC. *IEEE Journal of Solid-State Circuits*, 42(12):2946–2959, 12 2007.
- [33] Emilia Noorsal, Kriangkrai Sooksood, Hongcheng Xu, Ralf Hornig, Joachim Becker, and Maurits Ortmanns. A Neural Stimulator Frontend With High-Voltage Compliance and Programmable Pulse Shape for Epiretinal Implants. *IEEE Journal of Solid-State Circuits*, 47(1):244–256, 1 2012.
- [34] Hyung-Min Lee, Hangu Park, and Maysam Ghovanloo. A Power-Efficient Wireless System With Adaptive Supply Control for Deep Brain Stimulation. *IEEE Journal of Solid-State Circuits*, 48(9):2203–2216, 9 2013.
- [35] Elton Ho, Xin Lei, Thomas Flores, Henri Lorach, Tiffany Huang, Ludwig Galambos, Theodore Kamins, James Harris, Keith Mathieson, and Daniel Palanker. Characteristics of prosthetic vision in rats with subretinal flat and pillar electrode arrays. *Journal of Neural Engineering*, 16(6), 10 2019.
- [36] Daniel Palanker, Yannick Le Mer, Saddek Mohand-Said, Mahiul Muqit, and Jose A. Sahel. Photovoltaic Restoration of Central Vision in Atrophic Age-Related Macular Degeneration. *Ophthalmology*, 127:1097–1104, 2020.
- [37] Francesc Varkevisser, Tiago L Costa, and Wouter A Serdijn. Energy efficiency of pulse shaping in electrical stimulation: the interdependence of biophysical effects and circuit design losses. *Biomedical Physics & Engineering Express*, 8(6):065009, 11 2022.